

1 *This version of the article has been accepted for publication, after peer review (when*
2 *applicable) and is subject to Springer Nature's [AM terms of use](#), but is not the Version*
3 *of Record and does not reflect post-acceptance improvements, or any corrections. The*
4 *Version of Record is available online at: <http://dx.doi.org/10.1038/s41561-023-01291-3>*

5

6 **Title: Globally coherent water cycle response to temperature change during the past two**
7 **millennia**

8
9 **Authors:** Bronwen L. Konecky^{1*}, Nicholas P. McKay², Georgina M. Falster^{1,3}, Samantha L.
10 Stevenson⁴, Matt J. Fischer⁵, Alyssa R. Atwood⁶, Diane M. Thompson⁷, Matthew D. Jones⁸,
11 Jonathan J. Tyler⁹, Kristine L. DeLong¹⁰, Belen Martrat¹¹, Elizabeth K. Thomas¹², Jessica L.
12 Conroy¹³, Sylvia G. Dee¹⁴, Lukas Jonkers¹⁵, Olga V. Churakova (Sidorova)^{16,17}, Zoltán Kern^{18,19},
13 Thomas Opel²⁰, Trevor J. Porter²¹, Hussein R. Sayani²², Grzegorz Skrzypek²³, and Iso2k Project
14 Members[†]
15

16 **Affiliations:**

17 ¹Department of Earth and Planetary Sciences, Washington University, Saint Louis, Missouri,
18 63108, USA

19 ²School of Earth and Sustainability, Northern Arizona University, Flagstaff, AZ, 86011, USA

20 ³Research School of Earth Sciences and ARC Centre of Excellence for Climate Extremes,
21 Australian National University, Canberra, ACT, 2601, Australia

22 ⁴Bren School of Environmental Science & Management, University of California, Santa
23 Barbara, Santa Barbara, CA, 93106, USA

24 ⁵NST Environment, ANSTO, Sydney, NSW, 2234, Australia

25 ⁶Department of Earth, Ocean, and Atmospheric Sciences, Florida State University,
26 Tallahassee, Florida, 32306, USA

27 ⁷Department of Geosciences, University of Arizona, Tucson, Arizona, 85719, USA

28 ⁸School of Geography, University of Nottingham, Nottingham, NG7 2RD, UK

29 ⁹School of Physics, Chemistry and Earth Sciences, The University of Adelaide, Adelaide,
30 South Australia, 5005, Australia

31 ¹⁰Department of Geography and Anthropology, Coastal Studies Institute, Louisiana State
32 University, Baton Rouge, LA, 70803, USA

33 ¹¹Department of Environmental Chemistry, Institute of Environmental Assessment and
34 Water Research (IDAEA-CSIC), Barcelona, Barcelona, 08034, Spain

35 ¹²Department of Geology, University at Buffalo, Buffalo, NY, 14260, USA

36 ¹³Department of Geology, Department of Plant Biology, University of Illinois at Urbana-
37 Champaign, Urbana, IL, 61822, USA

38 ¹⁴Department of Earth, Environmental, and Planetary Sciences,, Rice University, Houston,
39 Texas, 77005, USA

40 ¹⁵MARUM Center for Marine Environmental Sciences, Bremen University, Bremen, 28359,
41 Germany

42 ¹⁶Institute of Ecology and Geography, Siberian Federal University, Krasnoyarsk, 660041,
43 Russian Federation

44 ¹⁷Department of Forest Dynamics, Swiss Federal Institute for Forest, Snow and Landscape
45 Research WSL, Birmensdorf, CH-8903, Switzerland

46 ¹⁸Institute for Geological and Geochemical Research, Research Centre for Astronomy and
47 Earth Sciences, Eötvös Loránd Research Network, Budapest, H-1112, Hungary

48 ¹⁹CSFK, MTA Centre of Excellence, Budapest, H-1121, Hungary

49 ²⁰Polar Terrestrial Environmental Systems, Alfred Wegener Institute Helmholtz Centre for
50 Polar and Marine Research, Potsdam, 14473, Germany

51 ²¹Department of Geography, Geomatics and Environment, University of Toronto -
52 Mississauga, Mississauga, Ontario, L5L1C6, Canada

53 ²²School of Earth and Atmospheric Science, Georgia Institute of Technology, Atlanta, GA,
54 30332, USA

55 ²³West Australian Biogeochemistry Centre, School of Biological Sciences, The University of
56 Western Australia, Perth, Western Australia, 6009, Australia

57
58
59

60 † Iso2k Project Members includes all above named authors and: Nerilie J. Abram (Australian
61 National University, Australia), Kerstin Braun (Arizona State University, USA), Matthieu
62 Carré (Sorbonne Universités (UPMC)-CNRS-IRD-MNHN, France), Olivier Cartapanis
63 (CEREGE, Aix Marseille Université, CNRS, IRD, INRAE, France), Laia Comas-Bru
64 (University of Reading, United Kingdom), Mark A. Curran (Australian Antarctic Division,
65 Australia), Emilie P. Dassié (University of Bordeaux, France), Michael Deininger (Johannes
66 Gutenberg University Mainz, Germany), Dmitry V. Divine (Norwegian Polar Institute,
67 Norway), Alessandro Incarbona (Palermo University, Italy), Darrell S. Kaufman (Northern
68 Arizona University, USA), Nikita Kaushal (University of Oxford, United Kingdom), Robert M.
69 Kläebe (The University of Adelaide, Australia), Hannah R. Kolus (Northern Arizona
70 University, USA), Guillaume Leduc (Aix Marseille University, CNRS, IRD, INRAE, Coll
71 France, CEREGE, France), Shreyas R. Managave (Indian Institute of Science Education
72 and Research, India), P. Graham Mortyn (Universitat Autònoma de Barcelona (UAB),
73 Spain), Andrew D. Moy (Australian Antarctic Division, Australia), Anais J. Orsi (Laboratoire
74 des Sciences du Climat et de L'Environnement, France), Judson W. Partin (University of
75 Texas at Austin, USA), Heidi A. Roop (University of Minnesota, USA), Marie-Alexandrine
76 Sicre (CNRS and Sorbonne Université, France), Lucien von Gunten (PAGES International
77 Project Office, Switzerland), and Kei Yoshimura (The University of Tokyo, Japan)

78
79

80 * Corresponding author. Email: bkonecky@wustl.edu

81
82

83

84

85

86

87

88

89

90 **The response of the global water cycle to changes in global surface temperature remains**
91 **an outstanding question in future climate projections and past climate reconstructions.**
92 **The stable hydrogen and oxygen isotope compositions of precipitation (δ_{precip}), meteoric**
93 **water (δ_{MW}), and seawater (δ_{SW}) integrate processes from microphysical to global scales**
94 **and thus are uniquely positioned to track global hydroclimate variations. Here, we**
95 **evaluate global hydroclimate during the past 2,000 years using a globally distributed**
96 **compilation of proxies for δ_{precip} , δ_{MW} , and δ_{SW} . We show that global mean surface**
97 **temperature exerted a coherent influence on global δ_{precip} and δ_{MW} throughout the past**
98 **two millennia, driven by global ocean evaporation and condensation processes, with**
99 **lower values during the Little Ice Age (1450-1850) and higher values after the onset of**
100 **anthropogenic warming (~1850). The Pacific Walker Circulation is a predominant source**
101 **of regional variability, particularly since 1850. Our results demonstrate rapid adjustments**
102 **in global precipitation and atmospheric circulation patterns – within decades – as the**
103 **planet warms and cools.**

104

105 Recent global syntheses of paleoclimate “proxy” data have constrained global mean surface
106 temperature (GMST) changes during the past 2000 years (i.e., the Common Era, CE), providing
107 critical context for anthropogenic warming^{1,2}. Yet despite the importance of water resources to
108 society, contemporaneous variations in the global water cycle — including precipitation,
109 evapotranspiration, atmospheric circulation, and modes of climate variability that affect these
110 processes — remain underconstrained^{3,4}.

111

112 Stable hydrogen and oxygen isotope ratios ($\delta^2\text{H}$ and $\delta^{18}\text{O}$) in environmental waters are well
113 positioned to provide a global picture of hydroclimate. Evaporation, condensation, freezing, and
114 other phase changes in the water cycle differentially impact (fractionate) heavy versus light
115 isotopes, causing the $\delta^2\text{H}$ and $\delta^{18}\text{O}$ of precipitation (δ_{precip}), precipitation-derived meteoric

116 waters such as lake and soil water (δ_{MW}), and seawater (δ_{SW}) to integrate and record
117 hydrological processes on timescales from minutes to millions of years^{5–12}. Variations in δ_{precip} ,
118 δ_{MW} , and δ_{SW} are subsequently incorporated into diverse geologic materials including
119 speleothem and coral carbonate, glacial ice, and tree cellulose. By synthesizing such data from
120 a variety of sources, it is therefore possible to infer changes in a powerful suite of hydroclimatic
121 variables: δ_{precip} , which reflects atmospheric factors such as condensation temperature,
122 precipitation amount, rainout history, and moisture source¹²; δ_{MW} from lake, soil, and
123 groundwaters, which reflects variations in δ_{precip} and surface water evaporation; and δ_{SW} , which
124 reflects δ_{precip} , seawater evaporation, and mixing^{13,14}.

125

126 We analyzed proxies for δ_{precip} , δ_{MW} , and δ_{SW} from the recently published PAGES Iso2k
127 database, which contains 759 globally-distributed paleoclimate records from coral, tree, ice,
128 speleothem, lake, and marine sites¹⁵. The database includes extensive metadata designed to
129 facilitate cross-archive comparison, including interpretations from the original publications and
130 supplemented with information from a team of over 50 archive experts (see ref. ¹⁵ for details on
131 database design). Metadata fields include original climatic interpretations, proxy system
132 transformations, and the multiple environmental drivers of the isotopic composition of the
133 measured material in each record (hereafter “isotope interpretation”). Each record is further
134 classified into one of three primary isotope interpretation groups: 1) δ_{precip} ; 2) Effective Moisture
135 (EM), i.e., the balance between precipitation and evaporation, with higher EM reflecting higher
136 precipitation relative to evaporation; or 3) the *in situ* temperature of the environmental medium
137 during the formation of the proxy sensor or archive¹⁵ (we note most records in the temperature
138 category are marine carbonates whose $\delta^{18}O$ primarily reflects seawater temperature, with only
139 minor influence of δ_{SW} ¹⁶). Regional and global analyses were performed on these three isotope
140 interpretation groups to distinguish patterns in different reservoirs of the water cycle
141 (precipitation, surface water, seawater), without *a priori* assumptions about the climatic drivers

142 of each record's variability (e.g., upstream monsoon intensity, regional air temperature), which
143 are more subject to change as records are re-interpreted over time (Methods).

144

145 For each group we created composite records of global $\delta^{18}\text{O}$ anomalies relative to the 0–2000
146 mean ($\Delta^{18}\text{O}$), including $\delta^2\text{H}$ records scaled to $\delta^{18}\text{O}$ -equivalent variance, using a dynamic
147 compositing method that was previously employed to reconstruct paleotemperature in a manner
148 that robustly handles proxy timeseries of different lengths, resolutions, and coverage periods
149 (ref. ¹⁷ and Methods). In addition to calculating composites, we performed Principal Component
150 Analysis (PCA) on a subset of higher-resolution (i.e., ≤ 30 year bins) individual proxy records
151 with $>85\%$ temporal data coverage during the Last Millennium (LM; 850–1850) to reveal
152 dominant spatiotemporal modes of variability (Methods). We compared these results to an
153 ensemble of three full-forcing LM experiments with the water isotope-enabled Community Earth
154 System Model (iCESM)^{18–20}.

155

156 The three $\Delta^{18}\text{O}$ composites (Fig. 1) display similar patterns, with notable differences in the
157 magnitude of centennial-scale variability. During the first millennium, composite $\Delta^{18}\text{O}$ of δ_{precip} -
158 driven records (hereafter, composite $\Delta^{18}\text{O}_{\delta_{\text{precip}}}$) was relatively stable, whereas composite $\Delta^{18}\text{O}$
159 of EM- and temperature-driven records (composite $\Delta^{18}\text{O}_{\text{EM}}$ and $\Delta^{18}\text{O}_{\text{temp}}$) increased and
160 decreased, respectively. During the LM, all three composites show a monotonic trend from ~ 800
161 to ~ 1700 , and a reversal of that trend since the 19th century. These patterns broadly echo the
162 temporal evolution of GMST during the LM¹, but with different magnitudes depending on the
163 primary environmental interpretation of $\delta^{18}\text{O}$. From 1000 to 1850, a global cooling of $0.25 (\pm 7$
164 $0.1)^\circ\text{C}^{-1}$ corresponds to a change of $-0.27 (\pm 0.00021)$, $+0.02 (\pm 0.00019)$, and $+0.09\text{‰} (\pm$
165 $0.0002)$ in composite $\Delta^{18}\text{O}_{\delta_{\text{precip}}}$, $\Delta^{18}\text{O}_{\text{EM}}$, and $\Delta^{18}\text{O}_{\text{temp}}$, respectively (Fig. 1A-C). Subsequent
166 warming of $0.65 (\pm 0.06)^\circ\text{C}$ from 1850 to 2000 corresponds to a change of $+0.56 (\pm 0.00012)$,

167 +0.62 (\pm 0.00017), and -0.16‰ (\pm 0.00023), respectively. Uncertainties in these estimates are
168 based on differences between the respective time periods across the full ensemble (Methods).
169
170 Composite $\Delta^{18}\text{O}_{\text{EM}}$ displays pronounced centennial-scale variability, with distinct positive
171 excursions from 300–500, 700–900, and 1800–2000. Variability in composite $\Delta^{18}\text{O}_{\text{EM}}$ is at least
172 twice the magnitude of composite $\Delta^{18}\text{O}_{\text{temp}}$ or $\Delta^{18}\text{O}_{\delta\text{precip}}$ (Fig. 1), likely due to the strong
173 influence of surface-water evaporation on lake and seawater $\delta^{18}\text{O}$, which amplifies the δ_{precip}
174 signal relative to noise^{11,12}.

175
176 The first principal component (PC1) of each category of records is dominated by a monotonic
177 trend over the LM, with smaller centennial-scale fluctuations (Fig. 2A). Similar to the
178 composites, the gross trend in each PC1 corresponds to a decrease in GMST. Site loadings on
179 each PC1, however, differ by region and by the primary environmental driver of $\delta^{18}\text{O}$ (Fig. 2B-
180 D). For example, positive trends and negative PC1 loadings are evident in $\delta^{18}\text{O}_{\text{temp}}$ at almost all
181 extra-tropical locations (Fig. 2D), consistent with the impact of ocean cooling on the $\delta^{18}\text{O}$ of
182 marine carbonates. Contrastingly, trends are insignificant in the Indo-Pacific Warm Pool where
183 $\delta^{18}\text{O}_{\text{sw}}$ influence likely confounds the temperature signal²¹.

184

185 **Influence of temperature on global δ_{MW}**

186 Together, the $\Delta^{18}\text{O}$ composites and PC1 suggest that GMST exerts a first-order control on
187 temporal changes in global δ_{MW} during the CE. The relationship of composite $\Delta^{18}\text{O}_{\delta\text{precip}}$ with
188 temperature is $0.68 \pm 0.20 \text{‰}/^{\circ}\text{C}$ for the full CE and $0.78 \pm 0.19 \text{‰}/^{\circ}\text{C}$ from 850-2000, based on
189 regression of the 30-year binned values (Methods) (Fig. 1A). A positive relationship between
190 GMST and δ_{precip} may be expected from high latitude ice cores^{12,22,23}, but positive relationships
191 in composite $\Delta^{18}\text{O}_{\delta\text{precip}}$ persist even when such records are excluded (Extended Data Fig. 1),
192 and also occur at mid and low latitudes, especially after 1850 (Extended Data Fig. 2). In

193 addition to the composites, the positive relationship between δ_{precip} and GMST is evident in PC1
194 of the δ_{precip} records spanning the entire CE (Extended Data Fig. 3A-B) and in iCESM
195 simulations (Fig. 3A,D; Extended Data Fig. 4). In iCESM, the regression slope between GMST
196 and global, 30-year smoothed, mean annual $\delta^{18}\text{O}_{\text{precip}}$ from 850-2000 is 0.25‰/°C, and
197 0.48‰/°C when calculated using Iso2k site locations (which, for δ_{precip} records, excludes nearly
198 all ocean grid cells and regions where site-level regression slopes are close to 0; Extended Data
199 Fig. 4). The iCESM slopes are shallower than in the Iso2k data, but the global slope is
200 consistent with earlier GCM estimates of 0.3‰/°C during the last deglaciation²⁴ and simplified
201 model estimates of zonal-mean temporal slopes of ~0.1-0.4‰/°C for most latitudes²⁵. The
202 discrepancy between the Iso2k and iCESM temporal slopes may reflect model biases in
203 extratropical moisture transport and positive $\delta^{18}\text{O}_{\text{precip}}$ biases at the high latitudes¹⁸. However,
204 the global temporal slope between GMST and $\delta^{18}\text{O}_{\text{precip}}$ has not been quantified
205 observationally— unlike spatially-derived slopes between site-level air temperature and
206 $\delta^{18}\text{O}_{\text{precip}}$ ^{11,12,22}— because modern $\delta^{18}\text{O}_{\text{precip}}$ measurements in most regions are either absent or
207 too short and discontinuous (most records <10 years) to do so beyond the scale of a few
208 years^{26,27}. Despite differences in magnitude, both iCESM and Iso2k data demonstrate that a
209 positive relationship between GMST and δ_{MW} is a persistent feature of the global water cycle for
210 the CE. The 30-year-binned Iso2k temporal slope of 0.68 ± 0.20 ‰/°C should be considered a
211 benchmark to be tested as longer observations and reanalyses become available.

212
213 Ice core and marine sediment studies have long recognized the importance of air temperature in
214 driving high latitude δ_{MW} , and of global ice volume in driving global δ_{SW} , on glacial-interglacial
215 timescales and across the Cenozoic^{12,23}. However, the nature of this relationship has remained
216 uncertain on the shorter (decadal to centennial) timescales most relevant for understanding
217 modern climate change and its impacts on water resources. Our results provide the first
218 observational evidence that GMST drives temporal changes in δ_{MW} and δ_{SW} , and therefore

219 changes in the hydrological cycle, on such timescales. Mechanisms other than global ice
220 volume, which has not changed substantially during the CE, are therefore required to explain
221 this relationship.

222

223 Although the Iso2k analyses are the first to document it, stable isotope theory and experimental
224 studies provide ample foundation for a positive imprint of GMST on global δ_{MW} , which is what our
225 spatially-distributed (albeit not spatially continuous) proxy network approximates. At the global
226 scale, a relationship between δ_{MW} and GMST will integrate all processes that relate local-scale
227 δ_{MW} with GMST, while balancing out regional distributions of heavy vs. light isotopologues
228 throughout the water cycle. Variations in global δ_{MW} therefore reflect variations in the isotopic
229 composition of the global oceanic and atmospheric reservoirs. Atmospheric δ_{vapor} is ultimately
230 governed by the isotopic composition of water evaporated from the oceans. Equilibrium
231 fractionation is greater at lower temperatures^{12,28}, so in a cooler world, the liquid-to-vapor
232 difference in $\delta^{18}O$ is higher than in warmer conditions (i.e., lower δ_{vapor} in the saturated
233 atmospheric layer above the ocean surface). Kinetic fractionation further decreases atmospheric
234 δ_{vapor} as newly evaporated vapor diffuses and mixes into the undersaturated free atmosphere,
235 with stronger fractionation when the lower troposphere is less humid^{29,30}. A globally cooler and
236 drier troposphere should therefore decrease δ_{vapor} to a greater extent than a warmer and more
237 humid troposphere. Global δ_{vapor} is further modified by temperature-dependent fractionation as
238 precipitation forms and condensation preferentially removes ^{18}O and decreases δ_{vapor} , with
239 greater isotopic discrimination at colder condensation temperatures^{12,28}.

240

241 iCESM simulations indicate multiple mechanisms play a role (Fig. 3). Higher GMST is
242 associated with higher $\delta^{18}O$ of water vapor flux from evaporating seawater into the saturated
243 boundary layer (0.14‰/°C), following the Craig-Gordon model^{13,31}, slightly higher relative
244 humidity with respect to sea surface temperature (0.77‰/°C) (Methods), and ultimately, higher

245 atmospheric $\delta^{18}\text{O}_{\text{vapor}}$ ($0.30\text{‰}/^\circ\text{C}$). Global δ_{precip} therefore reflects not only the δ_{vapor} determined
246 during ocean evaporation and mixing into the free atmosphere, but also the subsequent
247 depletion of ^{18}O in atmospheric vapor in the atmosphere through condensation, which via
248 equilibrium fractionation is stronger in a cooler climate. Stronger depletion of heavy isotopes in
249 precipitation also occurs with more vigorous circulation and shorter residence time of
250 atmospheric moisture³². For precipitation integrated over the timescales of most proxy systems
251 (weeks to months), δ_{precip} could become even lower when global precipitation rates are high
252 relative to the amount of precipitable water in the atmosphere, and higher when atmospheric
253 humidity increases to a greater extent than precipitation rate, as in the 20th century (Fig. 3; ref.
254 ³³).

255

256 Theory and simplified model experiments suggest that a cooler global atmosphere could also
257 favor stronger latitudinal gradients in δ_{precip} ¹², as lower temperatures increase distillation along
258 the water's path from the subtropics to the poles^{22,34}. A cooler atmosphere may also shift
259 evaporative source regions equatorward, driving a greater fraction of high latitude precipitation
260 to be sourced remotely²⁵ which strongly affects δ_{precip} at those latitudes³⁵. The latitudinal gradient
261 in Iso2k δ_{precip} records between 40° to 70° N and S is approximately -0.48‰ per degree latitude,
262 in agreement with observed modern slopes of ~ -0.3 to -0.6‰ per degree latitude^{22,34}. However,
263 we observe no difference in this gradient between the Little Ice Age and the 20th century — the
264 globally coldest and warmest intervals of the CE, respectively^{1,36} (Extended Data Fig. 5). Hence,
265 either equator-to-pole Rayleigh distillation is counterbalanced by changes in spatial patterns of
266 global evaporative recharge and moisture transport relative to precipitation^{25,35}, or the spread in
267 Iso2k δ_{precip} records is too large to resolve changing gradients during the LM when temperature
268 changes are relatively small. As spatial gradients are averaged out at the global scale, further
269 experiments with both simplified models and isotope-enabled GCMs are needed to

270 quantitatively decompose the relative importance of ocean evaporation, condensation, and
271 global precipitation and evaporation patterns on the global-scale GMST- δ_{precip} relationship.

272

273 **Patterns of regional variability**

274 Despite its influence on global mean δ_{MW} , GMST explains neither the spatial patterns nor the
275 shorter-term variability in δ_{MW} and δ_{SW} (Fig. 2, Extended Data Fig. 6). Instead, site-level PC1
276 loadings, LM trends, and centennial anomalies in $\delta^{18}\text{O}_{\delta\text{precip}}$ and $\delta^{18}\text{O}_{\text{EM}}$ are spatially
277 heterogeneous (Figs. 1-2, Extended Data Fig. 7). Although non-climatic processes and noise
278 likely contribute to this variability, this result also indicates that regional water balance,
279 atmospheric circulation, and precipitation characteristics dominate regional δ_{MW} not just in the
280 late 20th/early 21st centuries^{26,27} but also on multi-decadal to millennium-long timescales. In the
281 Arctic and the tropical Andes, negative trends in $\delta^{18}\text{O}_{\delta\text{precip}}$ and positive PC1 loadings agree with
282 documented Little Ice Age climate changes: high-latitude cooling, which lowered δ_{precip} in the
283 Arctic³⁷, and intensification of the South American summer monsoon, which lowered δ_{precip} in the
284 Andes³⁸. In eastern China and the Maritime Continent, positive PC1 loadings and negative
285 trends in $\delta^{18}\text{O}_{\delta\text{precip}}$ and $\delta^{18}\text{O}_{\text{EM}}$ over the LM indicate increasing effective moisture, with depletion
286 of heavy isotopes at some sites enhanced by intensifying convection and moisture transport
287 within the East Asian and Australasian summer monsoons^{39,40}. In northwestern North America
288 and Central America, negative PC1 loadings and positive trends in $\delta^{18}\text{O}_{\delta\text{precip}}$ and $\delta^{18}\text{O}_{\text{EM}}$
289 indicate increasing $\delta^{18}\text{O}_{\text{MW}}$ and declining EM over the LM, while southwestern North America
290 shows the opposite pattern, consistent with other LM proxy reconstructions^{41,42}. $\delta^{18}\text{O}_{\text{EM}}$ from
291 lakes exhibit the clearest trends in western North America, likely because δ_{precip} in the western
292 North American interior is especially sensitive to changes in water balance²⁷ and enhanced
293 evaporation during dry periods then amplifies increases in lake water $\delta^{18}\text{O}$. This explains why
294 coherent patterns emerge in western North American isotopic proxy records despite substantial
295 heterogeneity in compilations that blend isotopic and non-isotopic records⁴².

296
297 Opposing precipitation anomalies between southwestern North America and Central Asia
298 versus the Maritime Continent and South Asia during the LM have previously been attributed to
299 variability in the El Niño-Southern Oscillation⁴³, the interannual component of the east-west
300 atmospheric overturning circulation over the tropical Pacific known as the Pacific Walker
301 Circulation (PWC)⁴⁴. An underlying influence of the PWC may also explain some of the regional
302 coherency in Iso2k δ_{MW} . In modern precipitation, strengthening and weakening of the PWC
303 drives opposing precipitation and $\delta^{18}\text{O}_{\text{precip}}$ anomalies in Asia and the Americas due to changes
304 in precipitation amount, moisture source, and transport pathways²⁶. For example, rerouting of
305 the jet stream during El Niño events alters Pacific Ocean moisture trajectories toward
306 southwestern rather than northwestern North America^{45,46}. To the extent that these relationships
307 persist beyond interannual timescales, changes in moisture transport and EM provide a
308 plausible mechanism for multidecadal to centennial patterns in Asian and western North
309 American $\delta^{18}\text{O}_{\text{EM}}$.

310
311 Evidence for the PWC's influence on Iso2k records is stronger on sub-decadal timescales
312 during the historical period (1850–2005), when instrumental observations are available for direct
313 comparison. We correlated PC1 of 3-year binned Iso2k EM records with observed sea level
314 pressure (SLP) and found that the associated pattern mimics the observed global expression of
315 the PWC (Fig. 4a). Similarly, in iCESM experiments, PC1 of soil water $\delta^{18}\text{O}$ ($\delta^{18}\text{O}_{\text{soil}}$) at Iso2k
316 EM sites displays an SLP pattern that resembles iCESM's PWC (Fig. 4b). There is vigorous
317 debate surrounding the extent to which the PWC fluctuates on multidecadal and longer
318 timescales, either due to internal variability in the climate system or to external forcing^{47–50}. Our
319 results suggest that the PWC was the predominant influence on interannual $\delta^{18}\text{O}_{\text{precip}}$ not only
320 from 1982 to 2015²⁶, but at least since 1850, and likely on multi-decadal timescales prior to
321 1850.

322

323 Our results reveal a remarkably consistent relationship between GMST and δ_{MW} throughout the
324 CE, despite relatively constant ice-ocean boundary conditions. Between 1850-2000, global
325 δ_{precip} increased by at least 0.56‰, indicative of a warmer, more humid troposphere. Global δ_{MW}
326 and regional δ_{MW} appear to adjust to changing temperature and atmospheric circulation
327 patterns, respectively, within decades – similar to the timescale of the forcing itself. Expanded
328 δ_{MW} observational networks are critical for detecting and attributing shifts in rainfall, drought, and
329 circulation as the planet continues to warm.

330

331 **Acknowledgments**

332 Iso2k is a contribution to Phase 3 and 4 of the PAGES 2k Network. PAGES received support
333 from the Swiss Academy of Sciences, the US National Science Foundation, and the Chinese
334 Academy of Sciences. We thank three anonymous reviewers for helpful comments which
335 improved this manuscript.

336

337 Support for this work includes NSF-AGS 1805141, NSF-AGS PRF 1433408, and a David and
338 Lucile Packard Foundation Fellowship in Science and Engineering to BLK; NSF-1948746 to
339 NPM; Australian Research Council through a Discovery Project (DP170100557) and the Centre
340 of Excellence for Climate Extremes (CE170100023) to GMF; NSF-AGS 1805143 and NSF-
341 OCE-2202794 to SLS; NSF-CAREER 2145725, NSF 2103035, and NSF 2002444 to ARA;
342 NSF-CAREER 1945479, NSF 1931242, and NSF 2002460 to DMT; Australian Research
343 Council Discovery Project DP190102782 to JJT; South Central Climate Adaptation Science
344 Center Cooperative Agreement G19AC00086, NSF-2102931, and NSF-1805702 to KLD; RYC-
345 2013-14073 programme and LINKA20102 and CEX2018-000794-S projects to BM; NSF-EAR
346 PRF 1349595, NSF-EAR-IF 1652274, NSF-OPP 1504267, NSF-OPP 1737716, and NSF-
347 CAREER 2044616 to EKT; NSF-CAREER 1847791 to JLC; NOAA Award Number

348 NA18OAR4310427 to SGD; PalMod, the German paleoclimate modeling initiative, part of the
349 Research for Sustainable Development initiative funded by the German Federal Ministry of
350 Education and Research (BMBF; 01LP1922A) to LJ; RSF project 21-17-00006 to OVC(S);
351 German Research Foundation grants OP217/2-1, OP217/3-1, OP217/4-1 to TO; Natural
352 Sciences and Engineering Research Council of Canada Discovery Grant RGPIN-2016-06730 to
353 TJP; Australian Research Council Project (LP210300691) to GS; Australian Research Council
354 through a Future Fellowship (FT160100029), Special Research Initiative for the Australian
355 Centre for Excellence in Antarctic Science (SR200100008) and the Centre of Excellence for
356 Climate Extremes (CE170100023) to NJA.

357

358 **Author contributions**

359

360 Analyses presented in the main text and extended data were conceived and performed by BLK,
361 NPM, GMF, SS, MJF, AA, DMT, MDJ, JJT, EKT, JLC, SGD, and LJ.

362

363 Results were analyzed and interpreted by BLK, NPM, GMF, SS, MJF, AA, DMT, MDJ, KLD,
364 JJT, BM, and EKT, with input from all authors.

365

366 The manuscript was written mainly by BLK, NPM, GMF, SS, MJF, AA, DMT, MDJ, KLD, JJT,
367 BM, EKT, JLC, SGD, LJ, and HRS, with additional contributions from OVC, ZK, TO, TJP, and
368 GS.

369

370 All Iso2k Project Members created the Iso2k database and edited the manuscript.

371

372 BLK directed the project, led the overall design of the study, and led the writing of the
373 manuscript.

374

375 **Competing interests:**

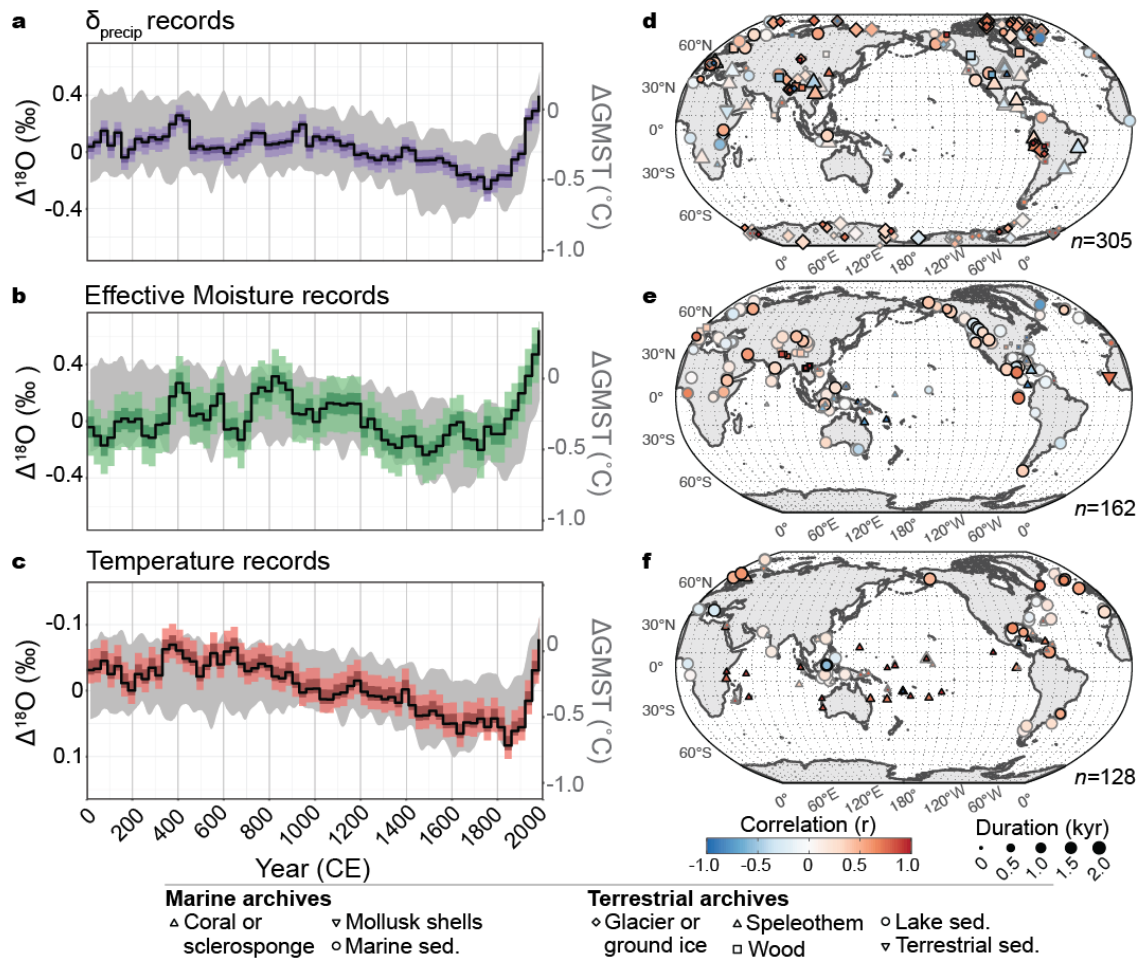
376

377 The authors declare no competing interests.

378

379

380 **Figures**



381

382 **Fig. 1. Global composite $\delta^{18}\text{O}$ anomalies.** a-c, 30-year binned proxy $\Delta^{18}\text{O}$ (black line,

383 ensemble median; dark shading, 25th–75th percentiles; light shading, 2.5th–97.5th percentiles) for

384 each group of Iso2k records¹⁵, anomalies relative to 2000-year mean. Gray shading depicts

385 ensemble 2.5th–97.5th percentile GMST anomaly relative to 1961-1990 mean¹. Note y-axis in (c)

386 is reversed to orient values upwards for warmer periods. **d-f**, Records contributing to each

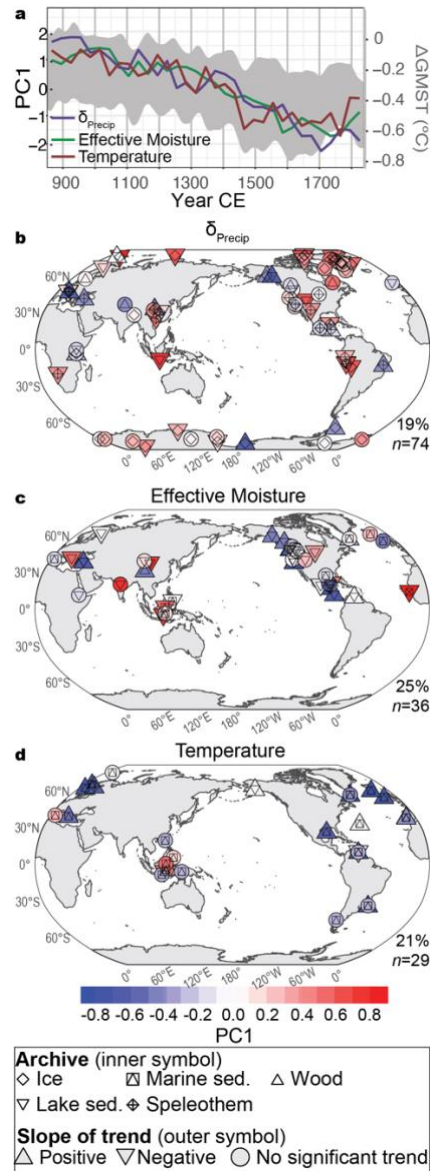
387 composite. Symbol shape, archive type; size, record duration; shading, correlation between that

388 record and the corresponding composite; bold outline, $p < 0.05$. Correlations are Pearson's r ,

389 two-sided, with no adjustment for multiple correlation. Maps created in R, using coastlines from

390 Natural Earth.

391



392

393 **Fig. 2. First principal components and trends in Iso2k records over the Last Millennium.**

394 **a**, PC1 of 30-year binned Iso2k¹⁵ records (850 to 1840), by interpretation group (colored lines),

395 compared to GMST anomaly (gray shading) as in Fig. 1. **b-d**, Spatial loadings on PC1 (symbol

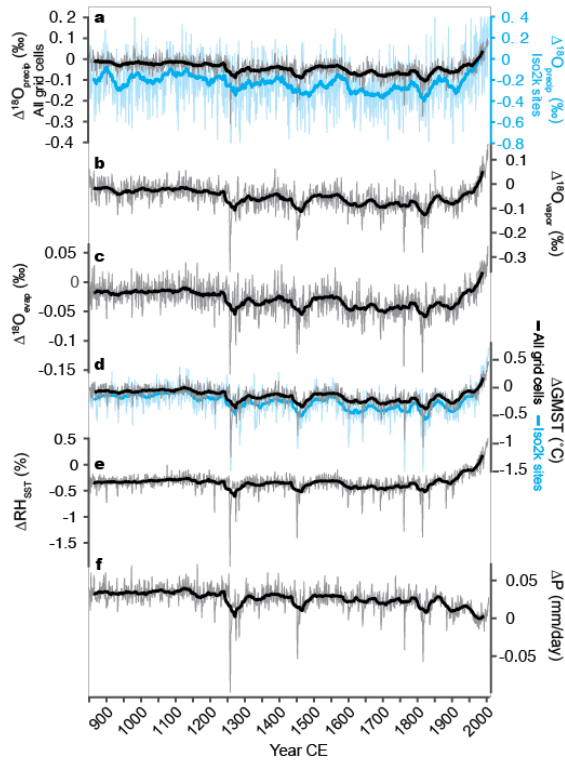
396 shading) for each group. Correlations are Pearson's *r*, two-sided, with no adjustment for multiple

397 correlation. Inner symbols, archive type; outer symbol shape, slope of significant ($p < 0.05$) linear

398 trend in the $\delta^{18}\text{O}$ of each individual record; labels, variance explained by PC1 and number of

399 records used. Maps created in R, using coastlines from Natural Earth.

400



401

402 **Fig. 3. Global hydroclimate and isotopic anomalies in iCESM^{18–20}.** **a**, Ensemble mean,

403 amount-weighted mean annual $\Delta^{18}\text{O}_{\text{precip}}$ anomaly relative to 1961 to 1990 mean (thin gray line)

404 and 30-year running mean (thick black line) for all grid cells, and for only grid cells containing

405 Iso2k site locations (blue lines). Note right Y axis in a is scaled 2x that of the left. **b-f**, as in **a**, but

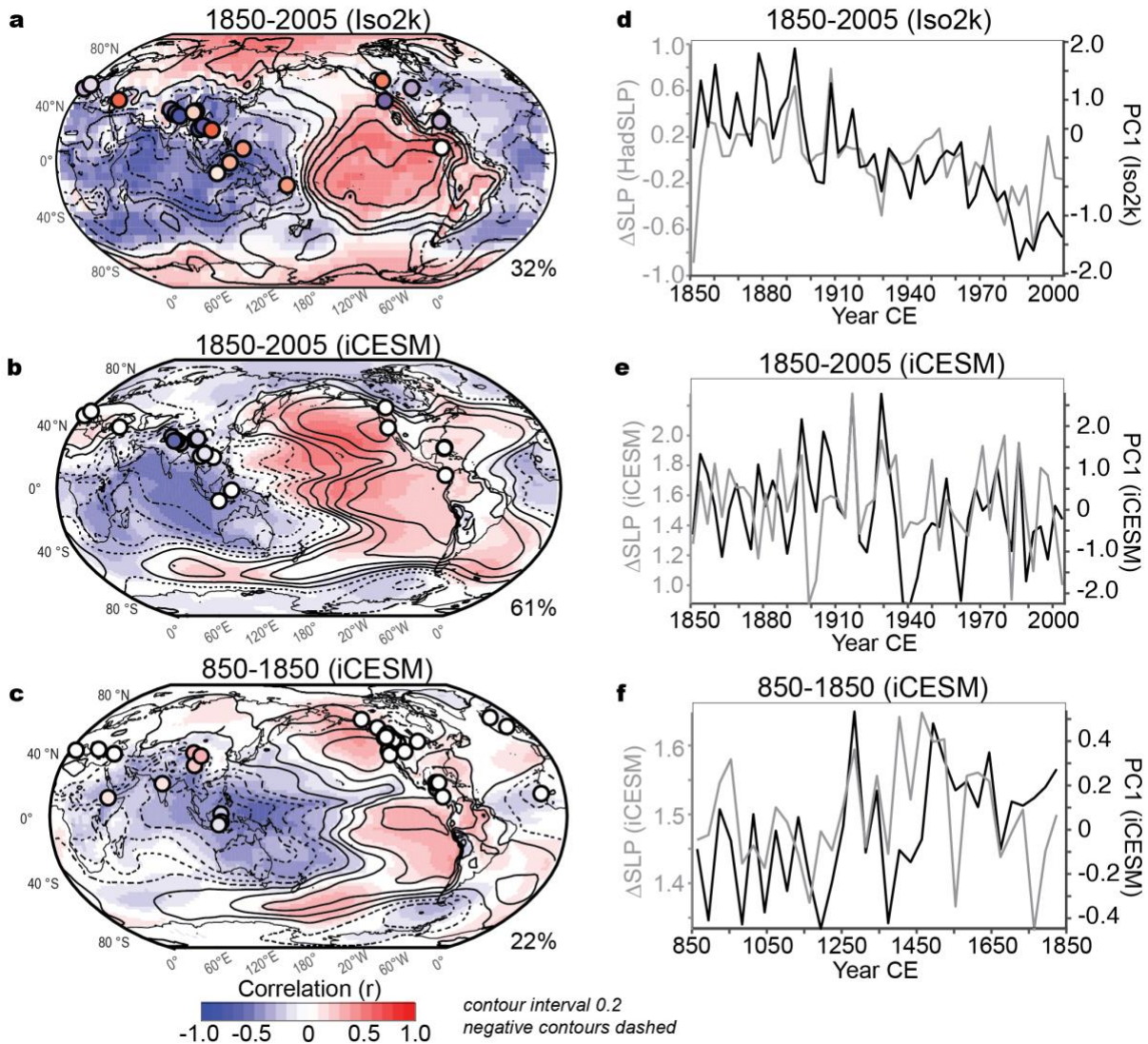
406 for **(b)** global column-averaged $\Delta^{18}\text{O}_{\text{vapor}}$, **(c)** $\Delta^{18}\text{O}$ of evaporative flux from the global oceans, **(d)**

407 GMST, **(e)** relative humidity over the low- and mid-latitude oceans (60°N-60°S), with respect to

408 saturation vapor pressure at sea surface temperature^{13,29,30}, and **(f)** global precipitation rate.

409

410



411
 412 **Fig. 4. Isotopic fingerprint of the Pacific Walker Circulation in Iso2k¹⁵ and iCESM¹⁸⁻²⁰.** a,
 413 Shading is the correlation between observed SLP and PC1 of 3-year binned Iso2k EM records
 414 (1850 to 2005). Symbol colors denote site loading on PC1. Unfilled contours denote correlation
 415 between SLP and PWC index Δ SLP. b, Correlation between SLP and ensemble-mean PC1 of
 416 3-year binned 0-10 cm $\delta^{18}\text{O}_{\text{soil}}$ in iCESM experiments (1850 to 2005), using grid cells of Iso2k
 417 EM sites (symbols). c, As in b, but for 30-year binned data from 850-1850. d-f, Time series of
 418 PC1 (black line) and Δ SLP (gray line) corresponding to panels a-c. Maps created in MATLAB
 419 using m_map for coastlines.

420

421 **References**

422

- 423 1. PAGES 2k Consortium. Consistent multidecadal variability in global temperature
424 reconstructions and simulations over the Common Era. *Nature Geoscience* **12**, 643–649
425 (2019).
- 426 2. PAGES 2k Consortium. A global multiproxy database for temperature reconstructions of the
427 Common Era. *Sci Data* **4**, 170088 (2017).
- 428 3. Field, C. B. *et al.* Part A: Global and sectoral aspects. Contribution of Working Group II to
429 the Fifth Assessment Report of the Intergovernmental Panel on Climate Change. in *Climate*
430 *Change 2014: Impacts, Adaptation, and Vulnerability* (Cambridge University Press, 2014).
- 431 4. Smerdon, J. E. *et al.* Comparing proxy and model estimates of hydroclimate variability and
432 change over the Common Era. *Proxy Use-Development-Validation/Terrestrial*
433 *Archives/Centennial-Decadal* (2017) doi:10.5194/cp-2017-37-RC1.
- 434 5. Rozanski, K. Isotopes in Atmospheric Moisture. in *Isotopes in the Water Cycle* (eds.
435 Aggarwal, P. K., Gat, J. R. & Froehlich, K. F.) 291–302 (Springer, 2005).
- 436 6. Galewsky, J. *et al.* Stable isotopes in atmospheric water vapor and applications to the
437 hydrologic cycle. *Reviews of Geophysics* **54**, 809–865 (2016).
- 438 7. Konecky, B. L., Noone, D. C. & Cobb, K. M. The Influence of Competing Hydroclimate
439 Processes on Stable Isotope Ratios in Tropical Rainfall. *Geophys. Res. Lett.* **46**, 1622–
440 1633 (2019).
- 441 8. Jasechko, S. Global isotope hydrogeology—review. *Rev. Geophys.* **57**, 835–965 (2019).
- 442 9. Sturm, C., Zhang, Q. & Noone, D. An introduction to stable water isotopes in climate
443 models: benefits of forward proxy modelling for paleoclimatology, *Clim. Past*, 6, 115--129.
444 Preprint at (2010).
- 445 10. Gat, J. *Isotope Hydrology: A Study of the Water Cycle*. vol. 6 (Imperial College Press,

- 446 2010).
- 447 11. Bowen, G. J., Cai, Z., Fiorella, R. P. & Putman, A. L. Isotopes in the Water Cycle: Regional-
448 to Global-Scale Patterns and Applications. *Annu. Rev. Earth Planet. Sci.* **47**, 453–479
449 (2019).
- 450 12. Dansgaard, W. Stable isotopes in precipitation. *Tellus* **16**, 436–468 (1964).
- 451 13. Craig, H. & Gordon, L. I. Deuterium and oxygen 18 variations in the ocean and the marine
452 atmosphere. in *Stable Isotopes in Oceanographic Studies and Paleotemperatures* (ed.
453 Tongiorgi, E.) 9–130 (Consiglio Nazionale Delle Ricerche, Laboratorio di Geologia Nucleare
454 - Pisa, 1965).
- 455 14. Rohling, E. J. PALEOCEANOGRAPHY, PHYSICAL AND CHEMICAL PROXIES | Oxygen
456 Isotope Composition of Seawater. in *Encyclopedia of Quaternary Science (Second Edition)*
457 (eds. Elias, S. A. & Mock, C. J.) 915–922 (Elsevier, 2013).
- 458 15. Konecky, B. L. *et al.* The Iso2k database: a global compilation of paleo- $\delta^{18}\text{O}$ and $\delta^2\text{H}$
459 records to aid understanding of Common Era climate. *Earth Syst. Sci. Data* **12**, 2261–2288
460 (2020).
- 461 16. Urey, H. C. Oxygen isotopes in nature and in the laboratory. *Science* **108**, 489–496 (1948).
- 462 17. Kaufman, D. *et al.* Holocene global mean surface temperature, a multi-method
463 reconstruction approach. *Sci Data* **7**, 201 (2020).
- 464 18. Brady, E. *et al.* The Connected Isotopic Water Cycle in the Community Earth System Model
465 Version 1. *Journal of Advances in Modeling Earth Systems* vol. 11 2547–2566 Preprint at
466 <https://doi.org/10.1029/2019ms001663> (2019).
- 467 19. Stevenson, S. *et al.* Volcanic Eruption Signatures in the Isotope-Enabled Last Millennium
468 Ensemble. *Paleoceanography and Paleoclimatology* **34**, 1534–1552 (2019).
- 469 20. Otto-Bliesner, B. L. *et al.* Climate Variability and Change since 850 CE: An Ensemble
470 Approach with the Community Earth System Model. *Bull. Am. Meteorol. Soc.* **97**, 735–754
471 (2016).

- 472 21. Thompson, D. M. *et al.* Identifying hydro-sensitive coral $\delta^{18}\text{O}$ records for improved high-
473 resolution temperature and salinity reconstructions. *Geophys. Res. Lett.* **49**, (2022).
- 474 22. Rozanski, K., Araguás-Araguás, L. & Gonfiantini, R. Isotopic patterns in modern global
475 precipitation. in *Climate Change in Continental Isotopic Records* (eds. Stewart, P. K.,
476 Lohmann, K. C., McKenzie, J. & Savin, S.) vol. 78 1–36 (American Geophysical Union,
477 1993).
- 478 23. Petit, J. R. *et al.* Climate and atmospheric history of the past 420,000 years from the Vostok
479 ice core, Antarctica. *Nature* **399**, 429–436 (1999).
- 480 24. Guan, J. *et al.* Understanding the temporal slope of the temperature-water isotope relation
481 during the deglaciation using isoCAM3: The slope equation. *J. Geophys. Res.* **121**, (2016).
- 482 25. Siler, N. *et al.* The large-scale, long-term coupling of temperature, hydrology, and water
483 isotopes. *J. Clim.* 1–51 (2021).
- 484 26. Falster, G., Konecky, B., Madhavan, M., Stevenson, S. & Coats, S. Imprint of the Pacific
485 Walker Circulation in Global Precipitation $\delta^{18}\text{O}$. *J. Clim.* **34**, 8579–8597 (2021).
- 486 27. Putman, A. L., Bowen, G. J. & Strong, C. Local and regional modes of hydroclimatic
487 change expressed in modern multidecadal precipitation oxygen isotope trends. *Geophys.*
488 *Res. Lett.* **48**, (2021).
- 489 28. Majoube, M. Fractionnement en oxygene 18 et en deuterium entre l'eau et sa vapeur.
490 *Journal de Chimie Physique* **68**, 1423–1436 (1971).
- 491 29. Craig, H., Gordon, L. I. & Horibe, Y. Isotopic exchange effects in the evaporation of water:
492 1. Low-temperature experimental results. *J. Geophys. Res. C: Oceans* **68**, 5079–5087
493 (1963).
- 494 30. Horita, J., Rozanski, K. & Cohen, S. Isotope effects in the evaporation of water: a status
495 report of the Craig-Gordon model. *Isotopes Environ. Health Stud.* **44**, 23–49 (2008).
- 496 31. Nusbaumer, J., Wong, T. E., Bardeen, C. & Noone, D. Evaluating hydrological processes in
497 the Community Atmosphere Model Version 5 (CAM5) using stable isotope ratios of water.

- 498 *J. Adv. Model. Earth Syst.* **9**, 949–977 (2017).
- 499 32. Aggarwal, P. K. *et al.* Stable isotopes in global precipitation: A unified interpretation based
500 on atmospheric moisture residence time. *Geophys. Res. Lett.* **39**, L11705 (2012).
- 501 33. Held, I. M. & Soden, B. J. Robust responses of the hydrological cycle to global warming. *J.*
502 *Clim.* **19**, 5686–5699 (2006).
- 503 34. Gat, J. R., Mook, W. G. & Meijer, H. A. *Environmental Isotopes in the Hydrological Cycle*,
504 *2nd ed.* vol. 2 (International Atomic Energy Agency, Vienna, Austria, 2001).
- 505 35. Bailey, A., Posmentier, E. & Feng, X. Patterns of evaporation and precipitation drive global
506 isotopic changes in atmospheric moisture. *Geophys. Res. Lett.* **45**, 7093–7101 (2018).
- 507 36. Neukom, R., Steiger, N., Gómez-Navarro, J. J., Wang, J. & Werner, J. P. No evidence for
508 globally coherent warm and cold periods over the preindustrial Common Era. *Nature* **571**,
509 550–554 (2019).
- 510 37. Stuiver, M., Grootes, P. M. & Braziunas, T. F. The GISP2 $\delta^{18}\text{O}$ Climate Record of the Past
511 16,500 Years and the Role of the Sun, Ocean, and Volcanoes. *Quat. Res.* **44**, 341–354
512 (1995).
- 513 38. Vuille, M. *et al.* A review of the South American Monsoon history as recorded in stable
514 isotopic proxies over the past two millennia. *Clim. Past* **8**, 1309–1321 (2012).
- 515 39. Zhao, K. *et al.* A high-resolved record of the Asian Summer Monsoon from Dongge Cave,
516 China for the past 1200 years. *Quat. Sci. Rev.* **122**, 250–257 (2015).
- 517 40. Konecky, B. L. *et al.* Intensification of southwestern Indonesian rainfall over the past
518 millennium. *Geophys. Res. Lett.* **40**, 386–391 (2013).
- 519 41. Cook, E. R., Seager, R., Cane, M. A. & Stahle, D. W. North American drought:
520 Reconstructions, causes, and consequences. *Earth-Sci. Rev.* **81**, 93–134 (2007).
- 521 42. Shuman, B. N. *et al.* Placing the Common Era in a Holocene context: millennial to
522 centennial patterns and trends in the hydroclimate of North America over the past 2000
523 years. *Clim. Past* **14**, 665–686 (2018).

- 524 43. Li, J., Xie, S.-P. & Cook, E. R. El Niño phases embedded in Asian and North American
525 drought reconstructions. *Quat. Sci. Rev.* **85**, 20–34 (2014).
- 526 44. Bjerknes, J. Atmospheric teleconnections from the equatorial Pacific. *Mon. Weather Rev.*
527 **97**, 163–172 (1969).
- 528 45. Kong, W. & Chiang, J. C. H. Southward shift of westerlies intensifies the east Asian early
529 summer rainband following El Niño. *Geophys. Res. Lett.* **47**, (2020).
- 530 46. Seager, R. *et al.* Adjustment of the atmospheric circulation to tropical Pacific SST
531 anomalies: Variability of transient eddy propagation in the Pacific-North America sector.
532 *Quart. J. Roy. Meteor. Soc.* **136**, 277–296 (2010).
- 533 47. Wittenberg, A. T. Are historical records sufficient to constrain ENSO simulations? *Geophys.*
534 *Res. Lett.* **36**, L12702 (2009).
- 535 48. Collins, M. *et al.* The impact of global warming on the tropical Pacific Ocean and El Niño.
536 *Nat. Geosci.* **3**, 391–397 (2010).
- 537 49. Vecchi, G. *et al.* Weakening of tropical Pacific atmospheric circulation due to anthropogenic
538 forcing. *Nature* **441**, 73–76 (2006).
- 539 50. Falster, G., Konecky, B., Coats, S. & Stevenson, S. Forced changes in the Pacific Walker
540 circulation over the past millennium. *Nature* (2023) doi:10.1038/s41586-023-06447-0.
- 541 51. Cheng, H. *et al.* Ice age terminations. *Science* **326**, 248–252 (2009).
- 542 52. Wang, Y. J. *et al.* A High-Resolution Absolute-Dated Late Pleistocene Monsoon Record
543 from Hulu Cave, China. *Science* **294**, 2345–2348 (2001).
- 544 53. Dayem, K. E., Molnar, P., Battisti, D. S. & Roe, G. H. Lessons learned from oxygen
545 isotopes in modern precipitation applied to interpretation of speleothem records of
546 paleoclimate from eastern Asia. *Earth Planet. Sci. Lett.* **295**, 219–230 (2010).
- 547 54. Osman, M. B., Coats, S., Das, S. B., McConnell, J. R. & Chellman, N. North Atlantic jet
548 stream projections in the context of the past 1,250 years. *Proc. Natl. Acad. Sci. U. S. A.*
549 **118**, (2021).

550 55. Hendricks. Space and time variation of $\delta^{18}\text{O}$ and δD in precipitation: Can
551 paleotemperature be estimated from ice cores? *Global Biogeochemical Cycles* (2000)
552 doi:10.1029/1999GB001198.

553 56. Liu, Z. *et al.* Younger Dryas cooling and the Greenland climate response to CO_2 .
554 *Proceedings of the National Academy of Sciences* **109**, 11101–11104 (2012).

555

556

557

558 **Methods**

559 **Disaggregation of analyses by isotope interpretation**

560 All global analyses presented in this paper are disaggregated by isotope interpretation rather
561 than by the original authors' climatic interpretation. This approach avoids building into our
562 synthesis *a priori* assumptions about the specific climatic variable driving $\delta^{18}\text{O}$ and $\delta^2\text{H}$
563 variability in each record, the basis for which is not always explained in the original publications.
564 In addition, many records contain multiple climatic interpretations (e.g., speleothem $\delta^{18}\text{O}$ being
565 driven mainly by monsoonal rainfall amount, but amplified by the ratio of summer vs. winter
566 moisture source changes^{51–53}), and the relative importance of each variable was impossible to
567 objectively evaluate for every time scale, region, and proxy system in the database. Finally,
568 climatic interpretations of isotope-based proxy records are continually evolving as new
569 information emerges from environmental monitoring and modeling studies (e.g., moisture
570 source and transport characteristics driving Greenland ice core $\delta^{18}\text{O}$ variability^{25,35,54–56};
571 seawater $\delta^{18}\text{O}$ driving coral $\delta^{18}\text{O}$ in some regions²¹). The isotope interpretation groupings are
572 less subject to interpretation because they chiefly represent isotope systematics and the
573 physical pools of environmental waters that each proxy sensor imbibes.

574

575 We separated δ_{precip} and EM records because EM proxies integrate information about
576 evaporation that is not expected from pure δ_{precip} proxies, which are mainly driven by factors
577 influencing condensation (e.g. air temperature, degree of rainout, import of moisture from
578 different sources)^{7,11}.

579

580 **Calculation of $\Delta^{18}\text{O}$ composites**

581 All records were extracted from the PAGES Iso2k Database v 1.0.0^{15,57}. The database contains
582 metadata on the principal determinants of isotopic composition in the measured material (e.g.,
583 the $\delta^{18}\text{O}$ of precipitation that forms glacial ice or cave dripwaters) and the record's climatic
584 interpretation (e.g., atmospheric temperature at condensation level, rainout due to monsoon
585 intensity), as interpreted by the original studies' authors and our team of archive experts¹⁵. For
586 each isotope interpretation group, we calculated an ensemble of 100 composite $\delta^{18}\text{O}$ time
587 series for the CE. Prior to calculation, we filtered the database to only include the 'primary' time
588 series for each site, and then grouped records according to the primary driver of isotopic
589 variability i.e., EM, temperature, or δ_{precip} ^{15,57}) (entitled 'EffectiveMoisture', 'Temperature', and
590 'P_isotope' in the 'isotopeInterpretation1_variableGroup' metadata field of the Iso2k database).

591

592 For records with isotope interpretation 'P_isotope', we also calculated separate composites for
593 a) glacier ice only, and b) excluding glacier ice (Extended Data Fig. 1). This separation was
594 performed to assess whether composite $\Delta^{18}\text{O}_{\delta_{\text{precip}}}$ is overprinted by the large number of ice
595 core records from high latitudes and high elevations, where temperature-driven isotopic
596 fractionation may disproportionately affect δ_{MW}^2 . An especially strong temperature- δ_{MW}
597 relationship may be unsurprising in the glacier ice $\delta^{18}\text{O}$ system. Glacier ice reflects δ_{precip} more
598 directly than other proxy sensors, which reflect pools of meteoric water (e.g. soil water and lake
599 water) that are influenced by precipitation and other secondary processes such as evaporation
600 or aquifer mixing. Glacier ice is found at high latitudes and altitudes, where cold temperatures

601 drive stronger stable isotope fractionation due to Rayleigh distillation and global patterns of
602 precipitation vs. evaporative recharge^{10–12,22,23,25,35,55}. Most of the glacier ice records included in
603 the Iso2k database are consistently interpreted as temperature indicators, and were included in
604 the PAGES 2k^{1,2} temperature database used for GMST calculations.

605

606 Despite these considerations, the observed global δ_{MW} -temperature relationship persists even
607 when glacier ice records are removed from the δ_{precip} composite (**Extended Data Fig. 1**), and in
608 low- and mid-latitudes where local temperature effects on δ_{precip} are small¹² (**Fig. 2**). The overall
609 patterns in PC1 are also similar regardless of whether glacier ice records are included or
610 excluded (**Extended Data Figs. 3, 8**). Therefore, the inclusion or exclusion of glacier ice
611 records does not substantially affect the composites or PCA, supporting that the strong
612 temperature- δ_{MW} relationship in our data is due to the overall influence of temperature on the
613 global pool of meteoric water and not due to the strong effect of air temperature on high-latitude
614 ice cores.

615

616 Records with ten or fewer data values within the CE were excluded from the analysis. $\delta^2\text{H}$
617 records ($n=45$ in composite $\Delta^{18}\text{O}_{\text{precip}}$, $n=12$ in composite $\Delta^{18}\text{O}_{\text{EM}}$) were divided by eight to
618 scale the magnitude of their variance with that of $\delta^{18}\text{O}$ in global meteoric waters⁵⁸. This was
619 done to avoid erroneously high apparent climate variability at $\delta^2\text{H}$ sites simply from the eight-
620 times-higher variability in $\delta^2\text{H}$ relative to $\delta^{18}\text{O}$, which arises from relative differences in
621 equilibrium fractionation factors between liquid and vapor for these isotope ratios⁵⁸. Local slopes
622 were not available for the 12 records from evaporative water bodies in composite $\Delta^{18}\text{O}_{\text{EM}}$, so the
623 global scaling of 8 was used.

624

625 Records in the Iso2k database have a wide variety of temporal resolution, length, and coverage
626 over the CE¹⁵. To align records to a common interval and resolution, the data were averaged

627 into equal bins of 30 years spanning the CE, which approximates the average resolution of the
628 lower resolution archive types in the database (marine and lake sediments). Records
629 contributing to each bin were mean-centered but not scaled by variance, as described below. To
630 minimize aliasing, the data were binned following a modified nearest-neighbor annual
631 interpolation procedure¹⁷. This approach accounts for the fact that for the non-annually-resolved
632 data, the age of a sample at a given depth typically represents more than one year of
633 accumulation (and up to several years or decades, or even longer for some low-resolution
634 sedimentary records), and may therefore contain climate information that is relevant to more
635 than one bin. The duration of each sample is not consistently recorded in the Iso2k database (or
636 the primary references), so to estimate sample coverage we calculated the distribution of gaps
637 between adjacent observations in each timeseries, and used nearest-neighbor interpolation to
638 estimate sample values spanning the intervals that are less than the 75th quantile of the
639 distribution of all gaps between adjacent observations (consistent with Kaufman et al.¹⁷).
640 Consequently, samples with resolution <30 years can potentially contribute to the weighted $\delta^{18}\text{O}$
641 calculation for up to two bins, though with less weight given to samples further from their
642 published age. In the case of records with resolution >30 years, this data-spreading step allows
643 observations to impact the composites across multiple bins, consistent with their interpretation
644 as multidecadal averages.

645

646 Record lengths also vary widely in the database, so there is no universal time period of common
647 overlap within the CE. We therefore aligned the records using the Dynamic Compositing
648 approach¹⁷, which uses randomly selected portions of each time series to adjust the $\delta^{18}\text{O}$
649 variance, then iteratively adjusts the mean $\delta^{18}\text{O}$ of each time series so that the mean of each
650 record is minimally offset from all other records in the composite. This process was repeated for
651 each of 100 ensemble members. Because the mean value of the records is adjusted during
652 compositing, the composite values are now in relative $\Delta^{18}\text{O}$ (in ‰), rather than in their original

653 $\delta^{18}\text{O}$ (or pre-scaled $\delta^2\text{H}$) values on the VSMOW-SLAP scale (i.e., in $1000\cdot\delta$ notation where 0‰
654 refers to standard mean ocean water). Therefore, for convenience, composite $\Delta^{18}\text{O}$ was slightly
655 shifted such that the mean of the ensemble median is 0‰. The final composite $\Delta^{18}\text{O}$ values
656 (**Fig. 1**) are therefore in units of ‰ anomalies relative to the 2000-year mean. Dynamic
657 compositing was used in ref. ¹⁷ to produce calibrated reconstructions of paleotemperature.
658 Unlike surface air temperature observations, long and complete timeseries of globally
659 distributed δ_{precip} , δ_{MW} , and δ_{SW} observations are insufficient (e.g. for δ_{precip} , large spatial
660 coverage gaps and few records longer than 10 years²⁶), and so calibrated reconstructions are
661 not possible until these observational networks are improved.

662

663

664

665 **PCA of Iso2k data**

666 We used PCA to calculate Empirical Orthogonal Functions (EOFs) from a subset of records in
667 the Iso2k database that met requirements for temporal coverage (described below; Fig. 2). Prior
668 to calculating the EOFs, we filtered the database as described for the $\Delta^{18}\text{O}$ composites, and
669 binned the raw data. PCA was performed using records in each of the three “isotope
670 interpretation” categories; for ‘P_isotope’ records, we performed separate PCA for a) glacier
671 ice, and b) ‘not glacier ice’ (i.e., all P_isotope records that are not from glacier ice). PCA was
672 performed on three temporal subsets: 0-1980 CE (30-year bins), 850-1840 (30-year bins), and
673 1850-2005 (3-year bins). Here we describe the methodology for the 850-1840 PCA that is
674 shown in the main text, then outline any adaptations that were made for the other two intervals.

675

676 Prior to PCA, all records were truncated to a fixed time interval of 850-1840. Other time
677 windows were explored and are presented in Extended Data Figs. 3 and 8. The 850-1840
678 interval was chosen in order to focus on pre-industrial variability, to avoid issues with records or

679 chronologies not extending fully to either the present day or the start of the CE, and to provide
680 comparison with LM model experiments from 850-1850. (Note a 990-year interval was used
681 because it is divisible by the 30-year bin size). Results of PCA on the 0-1980 interval (with 30-
682 year bins) and 1850-2005 (with 3-year bins) are shown in Extended Data Figs. 3 and 8. All data
683 processing for these intervals was as below.

684

685 Records included in the PCA had to meet stricter time coverage and completeness
686 requirements than records included in the composites. Binned records with <85% temporal
687 coverage during the 850-1840 interval were excluded. EOF analysis was carried out on the
688 matrix of remaining, screened time series using the Data Interpolation Empirical Orthogonal
689 Function (DINEOF) method, which accounts for records with a small number of missing data
690 points^{59,60}. DINEOF performs best when missing values are scattered randomly throughout the
691 input data time series. In the case of Iso2k records, missing data are generally concentrated at
692 the ends of records, and hence records with a large proportion of missing data have a large
693 impact on the PC loadings (though less impact on the overall PC time series). To check for
694 obvious artifacts induced by the data processing, we visually compared the binned and
695 interpolated records with their raw data equivalents. We performed the PCA on the binned and
696 interpolated data matrix using the `rda()` function of the 'vegan' package in R⁶¹. We scaled the
697 interpolated records to unit variance because they are from different proxy systems and hence
698 the raw data have widely ranging variance.

699

700 To test whether variability explained by the principal components could be explained
701 stochastically, we tested the magnitude of the eigenvalues against a stochastic null hypothesis,
702 using a block bootstrap method that accounts for decadal persistence (Extended Data Fig. 9).
703 For the 850-1840 analysis, we split all raw data records that contributed to the EOF into ten-
704 year blocks; we chose ten years because this separates interannual variance from interdecadal

705 persistence. For each time series, we randomly selected an initial block, identified all blocks with
706 similar means, and randomly sampled one block from these. The next selected block was the
707 successor to that randomly sampled block. Blocks with similar means were identified using
708 nearest neighbor-based ranking. For blocks with no successor (i.e., where there is a gap in the
709 time series), the successor block was randomly selected from all other blocks. The process was
710 then repeated 1000 times to produce an ensemble of time series. This method of re-sampling
711 preserves the effects of 1) irregular time spacing, 2) the autocorrelation function (to lags >30
712 years), and 3) the time series processing steps (e.g., binning) on the correlation structure of the
713 raw (unprocessed) time series. We followed exactly the same steps for the 0-1980 PCA, using a
714 30-year bin size.

715

716 The 1850-2004 PCA was performed using three-year bins, on records with 80% coverage.
717 Block bootstrap was performed using 3-year blocks because 10-year blocks were too coarse for
718 this short time period. As with the above, records were binned and standardized but not
719 detrended.

720

721 **PCA with iCESM experiments**

722 To compare the iCESM with Iso2k results, we performed PCA of 30-year binned iCESM surface
723 soil water $\delta^{18}\text{O}$ ($\delta^{18}\text{O}_{\text{soil}}$) i.e. the model variable most comparable to evaporation-sensitive
724 systems such as lakes. We used data from Iso2k EM site locations, spanning 850-1850, and
725 then regressed the ensemble-mean first PC against model SLP. The binned $\delta^{18}\text{O}_{\text{soil}}$ was
726 calculated for gridpoint time series corresponding to the “effective moisture” sites, taken from
727 each isotope-enabled Last Millennium Ensemble full-forcing ensemble member from the upper
728 0-10 cm of the soil profile in iCLM, then averaged to produce an ensemble mean. The upper 10
729 cm were chosen because in the model, isotopic fractionation is clearest at this level whereas
730 $\delta^{18}\text{O}_{\text{soil}}$ of deeper soil layers rapidly approaches $\delta^{18}\text{O}_{\text{precip}}$ ^{18,62}. EOF analysis was performed

731 using $\delta^{18}\text{O}_{\text{soil}}$ because the “lake” land cover type in iCLM4 is non-fractionating^{18,62} and hence no
732 model variable is available for direct comparison with the large number of lake-based Iso2k
733 $\delta^{18}\text{O}_{\text{EM}}$ proxies. Yet to first order, $\delta^{18}\text{O}_{\text{soil}}$ is similarly controlled by both $\delta^{18}\text{O}_{\text{precip}}$ and surface
734 evaporation, and $\delta^{18}\text{O}_{\text{soil}}$ is also an adequate comparison to tree cellulose and speleothem
735 records in the Iso2k EM category.

736

737 **Correlations with sea level pressure and calculation of PWC index**

738 Observed SLP and ΔSLP for the correlations against Iso2k HP PC1 (Fig. 4) were taken from the
739 HadSLP2r dataset⁶³. Following the treatment of the Iso2k data, the HadSLP dataset was binned
740 to 3 years but not detrended or deseasonalized (Fig. 4).

741

742 The index for the trans-Pacific SLP gradient (ΔSLP) is defined as anomalies (from the monthly
743 climatology) in the difference between area-mean SLP over the central-eastern Pacific Ocean
744 (160°W-180°W, 5°S-5°N) and the western Pacific and eastern Indian Oceans (80°E-160°E,
745 5°S-5°N)⁴⁹. Positive ΔSLP values represent an increased zonal pressure gradient, and hence
746 stronger PWC (and vice versa). ΔSLP was calculated using HadSLP2r for comparisons with
747 Iso2k (Fig. 4).

748

749 **Magnitudes of change in composite $\Delta^{18}\text{O}$ and GMST**

750 To estimate the magnitude of change in the three composite $\Delta^{18}\text{O}$ time series, we subtracted
751 the composite $\Delta^{18}\text{O}$ value at 1000 CE from the composite $\Delta^{18}\text{O}$ value at 1850 CE, for all 100
752 composite ensemble members. We likewise calculated the difference between 2000 CE and
753 1850 CE. Similarly for estimating the change in GMST during this interval, we subtracted the
754 temperature anomaly at 1000 (1850) from the same at 1850 (2000), for all 7000 ensemble
755 members. In all cases, we report the mean and standard deviation of the distributions of
756 magnitudes of change.

757

758 **Calculation of isotope-temperature relationships in Iso2k data and iCESM experiments**

759 We calculated the relationship between composite $\Delta^{18}\text{O}_{\delta\text{precip}}$ (i.e., an approximation of
760 anomalies in the global mean $\delta^{18}\text{O}$ of precipitation, given the spatial distribution of 305
761 δ_{precip} -sensitive proxy records) and GMST between 850-2000. We binned all ensemble
762 members from the most recent reconstruction of CE GMST¹ to match the $\Delta^{18}\text{O}_{\delta\text{precip}}$
763 composite. We then calculated linear regressions for 10000 unique combinations of
764 composite $\Delta^{18}\text{O}_{\delta\text{precip}}$ ensemble member ($n = 100$) on GMST ensemble member ($n =$
765 7000), for the two time intervals. We report the mean and standard deviation of the
766 distribution of regression coefficients, for the two time intervals.

767

768 For iCESM, isotope/temperature relationships were calculated for 850-2000 (the period of
769 overlap with Iso2k composites) using area-weighted globally averaged, mean annual
770 surface temperature and area-weighted, amount-weighted, mean annual global average
771 $\delta^{18}\text{O}_{\text{precip}}$ from the ensemble-mean of three isotope-enabled Last Millennium Ensemble
772 full-forcing simulations. Before determining the regression slopes, we calculated 30-year
773 running means for both surface temperature and $\delta^{18}\text{O}_{\text{precip}}$ (Fig. 3). Regression slopes in
774 the main text are reported for GMST vs. two time series: global mean $\delta^{18}\text{O}_{\text{precip}}$ (using all
775 grid cells), and mean $\delta^{18}\text{O}_{\text{precip}}$ calculated only for grid cells containing locations of Iso2k
776 primary time series data contributing to the composites between 850-2000 CE.

777

778 Similarly, to estimate the amount of variance in individual Iso2k primary time series explained by
779 proxy estimates of global temperature (Extended Data Fig. 6), we calculated R^2 for the 30-year
780 binned data across the interval 1-2000, ignoring bins that contained no observations.
781 Correlations were only calculated if at least six bins overlapped the bins from the GMST
782 reconstruction.

783

784 **Calculation of Relative Humidity normalized to SST**

785 Relative humidity was calculated from iCESM experiments for all grid points over the oceans
786 from 60°N-60°S, i.e. the portion of the lower troposphere receiving the majority of evaporated
787 water from the surface oceans. RH_{SST} in Fig. 3 was calculated as the relative humidity of the
788 surface-most model layer, normalized to the saturation vapor pressure at the temperature of the
789 surface ocean rather than the air, following the physical principles of the Craig-Gordon model for
790 an evaporating water body^{13,29,30}. All global-mean time series in Fig. 3 are area-weighted.

791

792 **Calculation of trends**

793 Trends (Fig. 2) were calculated as the slope of the linear regression from 850-1840 for a subset
794 of Iso2k records meeting the following criteria: 1) designated 'primary time series', 2) containing
795 at least one data point in the first and last 50 years of the time interval; and 3) containing at least
796 20 data points over the full time interval (i.e., ≥ 50 year average resolution). For iCESM data,
797 trends were calculated as the slope of the linear regression for monthly data covering the 850-
798 1850 and 1850-2005 time intervals.

799

800 **200-year standardized anomalies**

801 We created standardized anomaly ('z score') maps to aid interpretation of temporal variability in
802 the composite time series (Extended Data Fig. 7). Similarly to the analyses described above, we
803 filtered the database to only include the 'primary' isotope ($\delta^{18}O$ or δ^2H) time series for each site,
804 and then grouped records according to the primary driver of isotopic variability. We then filtered
805 this subset of data sets to only include records spanning >600 years within the CE. We
806 averaged those records into 200-year bins, and then calculated z-scores for each bin by
807 subtracting the mean of all data points within the CE from the bin average, and then dividing by
808 the standard deviation of all data points within the CE. We performed this analysis using both

809 'odd' (100, 300, 500 etc.) and 'even' (200, 400, 600) centuries as bin centers and showed only
810 the time periods relevant to the main text in Extended Data Fig. 7.

811

812

813

814

815 **Data Availability Statement**

816 The Iso2k Database⁵⁷ is available for download at <https://doi.org/10.25921/57j8-vs18> and is
817 accessible via the NOAA/WDS Paleo Data landing page at
818 <https://www.ncdc.noaa.gov/paleo/study/29593>. Composites and principal components datasets
819 generated for this manuscript are available through Github
820 <https://github.com/nickmckay/iso2kNatureGeoscience2023> and archived via Zenodo (doi:
821 10.5281/zenodo.8327339).

822

823 **Code Availability Statement**

824 Codes to reproduce the main results from this manuscript are available through Github
825 <https://github.com/nickmckay/iso2kNatureGeoscience2023> and archived via Zenodo (doi:
826 10.5281/zenodo.8327339).

827

828 **Methods-only References**

829

830 57. Konecky, B. L. & McKay, N. P. NOAA/WDS Paleoclimatology - The Iso2k
831 Database. NOAA National Centers for Environmental Information. (2020)
832 doi:10.25921/57j8-vs18.

833 58. Craig, H. Isotopic Variations in Meteoric Waters. *Science* **133**, 1702–1703
834 (1961).

- 835 59. Beckers, J.-M., Barth, A. & Alvera-Azcárate, A. DINEOF reconstruction of
836 clouded images including error maps—application to the Sea-Surface Temperature around
837 Corsican Island. *Ocean Science* **2**, 183–199 (2006).
- 838 60. Alvera-Azcárate, A., Barth, A., Sirjacobs, D., Lenartz, F. & Beckers, J.-M. Data
839 Interpolating Empirical Orthogonal Functions (DINEOF): a tool for geophysical data
840 analyses. *Mediterr. Mar. Sci.* **12**, 5–11 (2011).
- 841 61. Oksanen, J., Kindt, R., Legendre, P. & Others. Vegan: community ecology
842 package. R package version 2.2-1. R Development Core Team, Vienna. Preprint at (2015).
- 843 62. Wong, T. E., Nusbaumer, J. & Noone, D. C. Evaluation of modeled land-
844 atmosphere exchanges with a comprehensive water isotope fractionation scheme in
845 version 4 of the Community Land Model. *J. Adv. Model. Earth Syst.* **9**, 978–1001 (2017).
- 846 63. Allan, R. & Ansell, T. A New Globally Complete Monthly Historical Gridded Mean Sea Level
847 Pressure Dataset (HadSLP2): 1850–2004. *J. Clim.* **19**, 5816–5842 (2006).